The selection of mixed-mode oscillations in a Hodgkin-Huxley model with multiple timescales

Jonathan Rubin
Department of Mathematics, University of Pittsburgh, Pittsburgh, Pennsylvania 15260, USA

Martin Wechselberger
School of Mathematics and Statistics, University of Sydney, Sydney, NSW 2006, Australia

In recent work [J. Rubin and M. Wechselberger, Biol. Cybern. **97**, 5 (2007)], we explained the appearance of remarkably slow oscillations in the classical Hodgkin-Huxley (HH) equations, modified by scaling a time constant, using recently developed theory about mixed-mode oscillations (MMOs). This theory is only rigorously valid, however, for ε sufficiently small, where ε is a parameter that arises from nondimensionalization of the HH system. Here, we illustrate how the parameter regime over which MMOs exist, and the features of the MMO patterns within this regime, vary with respect to several key parameters in the nondimensionalized HH equations, including ε. Moreover, we explain our findings in terms of the effects that these parameters are expected to have on certain organizing structures within the corresponding flow, generalized from analysis done previously in the singular limit. © *2008 American Institute of Physics*.
[DOI: 10.1063/1.2789564]

It is well known that the space-clamped Hodgkin-Huxley (HH) equations[1] exhibit stable periodic relaxation oscillations for a certain range of constant applied depolarizing current. Recent studies[2-6] have shown that a modified version of the HH equations, where only the speeds of the gating dynamics of the corresponding ion channels are changed, can lead to very slow firing rates of action potentials. In Ref. 6, we explained this observation and the corresponding complex oscillatory patterns, known as mixed-mode oscillations (MMOs), within the framework of multiple timescales analysis via the generalized canard phenomenon.[8] In this paper, we show how features of MMO patterns vary with respect to several key parameters in the modified HH equations. Moreover, the wide range of results that we numerically observe can be linked to the multiple timescales analysis, at least on a qualitative level.

I. INTRODUCTION

The Hodgkin-Huxley (HH) equations, which were derived empirically to describe the evolution of the membrane potential of the squid giant axon,[1] represent a rich source of interesting dynamics. The nondimensionalized Hodgkin-Huxley system

$$\varepsilon \frac{dv}{d\tau} = [\bar{I} - m^3 h(v - \bar{E}_{Na}) - \bar{g}_k n^4(v - \bar{E}_K) - \bar{g}_l(v - \bar{E}_L)],$$

$$\varepsilon \frac{dm}{d\tau} = \frac{1}{\tau_m t_m(v)}(m_\infty(v) - m),$$

$$\frac{dh}{d\tau} = \frac{1}{\tau_h t_h(v)}(h_\infty(v) - h),$$

$$\frac{dn}{d\tau} = \frac{1}{\tau_n t_n(v)}(n_\infty(v) - n), \tag{1}$$

was derived in Ref. 6 from a version of the classical HH equations obtained by introducing independent time constants τ_m, τ_h, τ_n in the conductance equations, as suggested in Refs. 2–5. The value of ϵ that results from this derivation is $1/120 \approx 0.0083$, which represents the reciprocal of the largest maximal ionic conductance, that of the sodium current, in the original model. The classical case thus corresponds to $\epsilon = 0.0083$, with $\tau_m = \tau_h = \tau_n = 1$ and with other parameter values and functional forms given in the Appendix (see also Ref. 6).

By setting $\epsilon = 0$ in system (1), we obtain the corresponding reduced (or slow sub-) system, describing the evolution of (h, n) on the two-dimensional manifold S_0 defined by

$$n^4(v, m, h) = \frac{\bar{I} - m^3 h(v - \bar{E}_{Na}) - \bar{g}_l(v - \bar{E}_L)}{\bar{g}_k(v - \bar{E}_K)}, \tag{2}$$

$$m(v, n, h) = m_\infty(v). \tag{3}$$

S_0 is a cubic shaped surface, $S_0 = S_a^- \cup L^- \cup S_r \cup L^+ \cup S_a^+$, featuring two attracting branches $S_a^\pm$, a repelling branch S_r, a fold L^- at which S_a^- and S_r meet, and a fold L^+ at which S_r and S_a^+ meet (see Fig. 1). In Ref. 6, we prove that system (1) possesses three-dimensional local center manifolds in a neighborhood of each of $L^\pm$, which are exponentially attracting. On each, the vector field is given by

$$\varepsilon \frac{dv}{d\tau} = [\bar{I} - m_\infty^3(v)h(v - \bar{E}_{Na}) - \bar{g}_k n^4(v - \bar{E}_K) - \bar{g}_l(v - \bar{E}_L)]$$
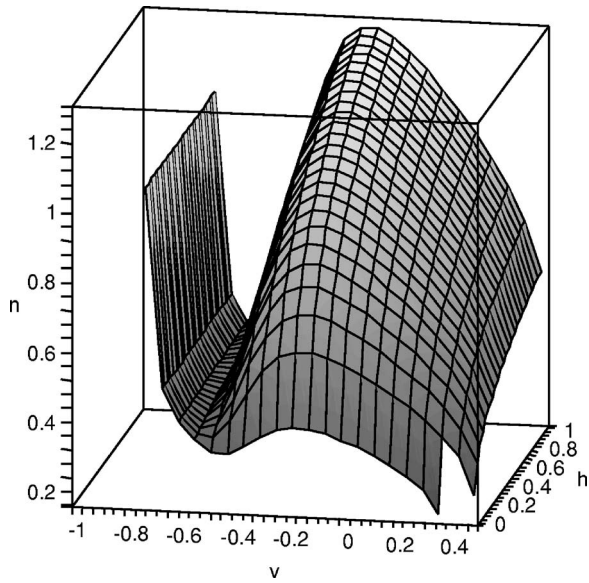
$$=: F(v, n, h),$$

FIG. 1. Cubic shaped critical manifold S_0 of the dimensionless HH system (1) with $I=9.6$, shown in (v,h,n) space. In this visualization, the left, center, and right branches of S_0 are S_a^-, S_r, and S_a^+, respectively, while the lower (upper) fold is L^- (L^+).

FIG. 2. An MMO that arises as a solution of the classical HH model, with additional time constants τ_m, τ_h, τ_n inserted in the m, h, n equations, respectively. Here, $\tau_m=1$, $\tau_h=3$, $\tau_n=1$, and $I=10.6$. Top: voltage time course featuring small oscillations between large excursions. Bottom: same solution projected to the (h,v) plane.

$$\frac{dh}{d\tau} = \frac{1}{\tau_h t_h(v)}(h_\infty(v) - h) =: H(v,h), \tag{4}$$

$$\frac{dn}{d\tau} = \frac{1}{\tau_n t_n(v)}(n_\infty(v) - n) =: N(v,n),$$

corresponding to simply setting $m=m_\infty(v)$ in Eq. (1), as specified in Eq. (3).

Remark 1.1: *Away from the fold lines, the manifolds S_a^- and S_a^+ are normally hyperbolic. Therefore, for ϵ sufficiently small, each of these perturbs, away from $L^\pm$, to a two-dimensional invariant manifold, and a global reduction of system (1) away from $L^\pm$ to a two-dimensional system on these manifolds is justified.*[7] *Since we are concerned with trajectories that approach $L^\pm$, however, we will work with Eq. (4).*

Past work has demonstrated that a step increase in τ_h or τ_n can lead to the existence of mixed-mode oscillations (MMOs), featuring alternating sets of large excursions and of small (or subthreshold) oscillations (STOs) in v, as solutions of the dimensional form of Eq. (1)[2–5] (see Fig. 2). In Ref. 6, we used recently developed mathematical theory[8,10,11] to explain the onset and offset of MMOs in system (4) under the systematic, independent variation of τ_h, τ_n, and I. For the parameter $\bar{I}$ that appears in Eq. (4), we have $\bar{I}=I/k$, where k is a particular constant that emerges from nondimensionalization (see the Appendix), and we vary I rather than $\bar{I}$ to allow for direct comparison with I values from the original HH equations.

In this paper, we consider how the values of τ_h and I, as well as the parameter ϵ, select the properties of the MMOs that arise in system (4). That is, a label L^s is applied to each MMO to characterize the number of large excursions (L) and small oscillations (s) that occur per cycle. We would like to know how the parameters in Eq. (4) contribute to the selec-
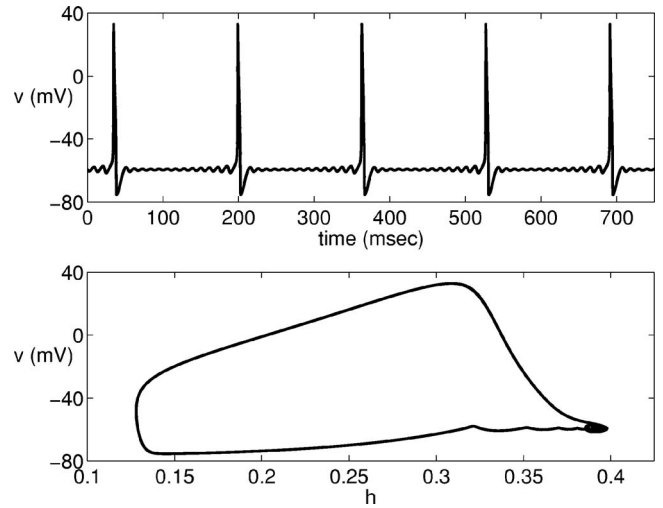
tion of L and s. Strictly speaking, the MMO theory that has been developed is valid close to the singular limit $\epsilon \downarrow 0$, and thus it is of interest to consider how the behavior of solutions changes as ϵ is made larger. Heuristically, increases in ϵ lead to a blurring between the fast and slow timescales in system (4), while increases in τ_h result in a separation between the timescales of the h- and n-dynamics, such that changes in ϵ and τ_h both offer the possibility of interesting effects that are outside of the existing rigorous theory. In addition to ϵ and τ_h, we consider the effects of varying I, since I represents a natural bifurcation parameter in the HH equations and variations in I can transition Eq. (4) from excitable to oscillatory, with MMOs arising along the way.[6] To keep the paper focused, we do not consider variation of τ_n here.[2–6]

In Sec. II, we list a set of assumptions that set up a structure that can allow for the existence of MMOs in general systems with one fast and two slow variables in $\mathbb{R}^3$. Further, we define certain quantities that are relevant to the existence and characteristics of MMOs, and we state fundamental existence theorems that were proven previously[8,10] for certain types of MMOs. In Sec. III, we use these theorems to consider the effect of ε on the values of I at which the onset and offset of MMOs occur for system (4), and we explain why, for $\varepsilon > 10^{-5}$, system (4) is outside the regime where these theorems rigorously apply. Section IV contains our results on how changes in ε, τ_h, and I affect the characteristics of MMOs for system (4). These results are presented through numerical experiments, accompanied by theoretical explanations. The theory here is stated in terms of the effects of parameters both on the local flow near transitions from small oscillations to large excursions and on the global return to this transitional region, extrapolated from rigorous results in the singular limit. The main points within these results are summarized in Sec. V.
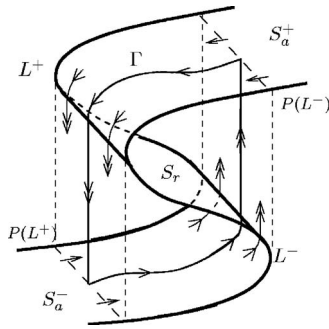
FIG. 3. Schematic illustration of a singular periodic orbit Γ on a critical manifold $S_0 = S_a^- \cup S_r \cup S_a^+$. Note that $L^\pm$ are folds of S_0 and that $P(L^\pm) \subset S_a^\mp$ are their projections to the opposite branches of S_0.

II. BRIEF SUMMARY OF RELEVANT MMO THEORY

Consider a three-dimensional system, such as Eq. (4), with singular perturbation parameter ϵ and with one fast and two slow variables. If the system has a cubic shaped critical manifold

$$S_0 = \{(v, h, n) \in \mathbb{R}^3 : F(v, n, h) = 0\},$$

then certain additional features ensure the existence of MMOs for ϵ sufficiently small. Essentially, MMOs arise when, for $\epsilon = 0$, there exists a singular periodic orbit that becomes trapped in a funnel structure, created by invariant manifolds of branches of S_0, near one of the folds of S_0. To make this more precise, and to set up notation that will be useful later in the paper, we state the following assumptions, which are also given in Ref. 6.

Assumption 1: The manifold $S := \{(v, h, n) \in S_0 : h \in [0, 1]\}$ is "cubic-shaped;" i.e., $S = S_a^- \cup L^- \cup S_r \cup L^+ \cup S_a^+$ with attracting upper and lower branches $S_a^\pm$, $S_a^+ \cup S_a^-$ $:= \{(v, h, n) \in S : F_v(v, h, n) < 0\}$, a repelling branch S_r $:= \{(v, h, n) \in S : F_v(v, h, n) > 0\}$ and fold curves $L^\pm$, $L^+ \cup L^-$ $:= \{(v, h, n) \in S : F_v(v, h, n) = 0, F_{vv}(v, h, n) \neq 0\}$; see Fig. 3.

Recall that the reduced system for Eq. (4) is obtained by setting $\epsilon = 0$. A layer (or fast sub-) system is obtained by rescaling to the fast time $\tau_1 = \tau / \varepsilon$ and then setting $\epsilon = 0$. Let $P(L^\mp) \subset S_a^\pm$ denote the projections of each of $L^\pm$ to the opposite attracting branch of S_0, along the fast fibers of the layer system (Fig. 3).

Assumption 2: There exists a singular periodic orbit Γ of Eq. (4) that is transversal to $P(L^\pm)$ on $S_a^\mp$. More specifically, $\Gamma = \Gamma_a^- \cup \Gamma_f^- \cup \Gamma_a^+ \cup \Gamma_f^+$ is a piecewise smooth closed curve that consists of solutions $\Gamma_a^\pm \subset S_a^\pm$ of the reduced system of Eq. (4), connecting points on the projection curves $P(L^\mp) \subset S_a^\pm$ to the fold curves $L^\pm$, concatenated with solutions $\Gamma_f^\pm$ of the layer system of Eq. (4), connecting points on $L^\pm$ to $P(L^\pm)$; see Fig. 3.

The reduced and layer systems represent the subsystems that emerge naturally from the separation of timescales in Eq. (4). However, a useful alternative reduction comes from noting that the critical manifold S_0 is given as a graph $n(v, h), h \in [0, 1], v \in \mathbb{R}$, along which $F(v, n, h) = 0$, based on Eqs. (2) and (3). The flow of the reduced system projected onto the (h, v) plane can be obtained from implicit differentiation of $F(v, n, h) = 0$, and is given by
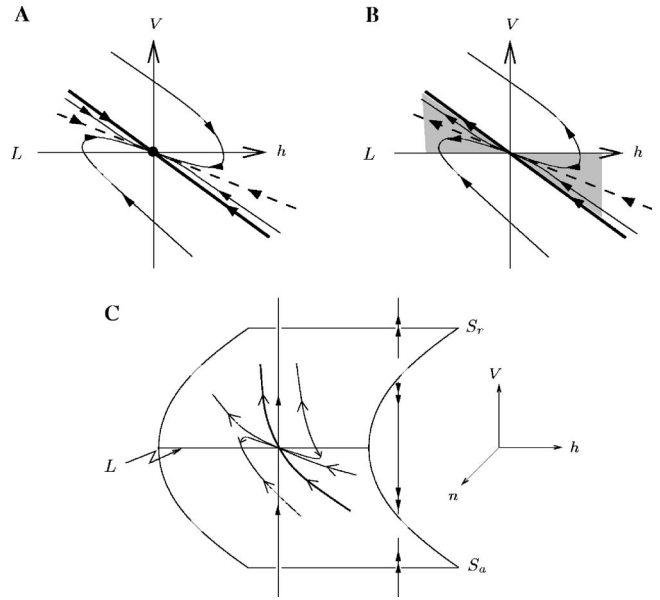

FIG. 4. Schematic illustration of the reduced flow near a folded node singularity. (A) Trajectories of the desingularized flow are aligned according to the strong (bold) and weak (dashed) stable eigendirections associated with the node. The fold L lies on the h axis. (B) In the reduced flow near the folded node singularity, all trajectories within the singular funnel on S_a, corresponding to the shadowed region satisfying $V < 0$, are funneled through the folded node singularity to S_r ($V > 0$). Note that the strong (bold) eigendirection shown is a linear approximation of the corresponding strong canard. (C) Three-dimensional representation of the reduced flow on the critical manifold.

$$\begin{pmatrix} \dot{h} \\ -F_v \dot{v} \end{pmatrix} = \begin{pmatrix} H \\ F_n N + F_h H \end{pmatrix}, \tag{5}$$

where F, H, and N are defined in Eq. (4). The equation for $\dot{v}$ is singular along the fold curves: $F_v = 0$. Therefore, we rescale time by $\tau \rightarrow t = \tau / (-F_v)$ to obtain the *desingularized reduced flow*

$$\begin{pmatrix} \dot{h} \\ \dot{v} \end{pmatrix} = \begin{pmatrix} -F_v H \\ F_n N + F_h H \end{pmatrix}, \tag{6}$$

where the overdot in Eq. (6) denotes differentiation with respect to the new time t. System (6) has the same phase portrait as the reduced system (5), but with the orientation of trajectories reversed on S_r.

Equilibria of system (6) can be classified into *regular singularities* and *folded singularities*. Regular singularities are given by $H = N = 0$, or equivalently, $n(v, h_\infty(v)) = n_\infty(v)$, which has a solution $v = v(I)$, independent of τ_h and τ_n. Folded singularities are given by $F_v = 0$, which ensures that they lie on one of $L^\pm$, and $F_n N + F_h H = 0$. These points depend on τ_h, τ_n, and I. Since $F_n \neq 0$ on the physiologically relevant domain, there are no equilibria with $H = 0$ and $N \neq 0$. Each folded singularity is classified as a folded node, folded saddle, or folded saddle-node, based on its classification as an equilibrium point of Eq. (6). Note that folded singularities are not equilibria of Eq. (5) but give the opportunity for the reduced flow to cross from S_a to S_r (a folded node is shown in Fig. 4). Finally, if a point on a fold is not a folded singularity, it is called a *jump point*.
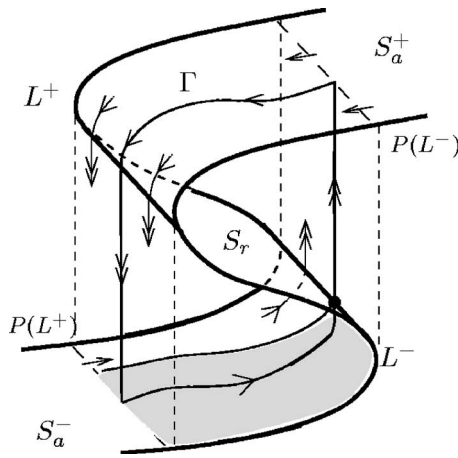
FIG. 5. Schematic illustration of a singular periodic orbit Γ on a critical manifold $S_0 = S_a^- \cup S_r \cup S_a^+$ that corresponds to a periodic orbit of MMO type 1^s for system (4) as described by Theorem 2.1.
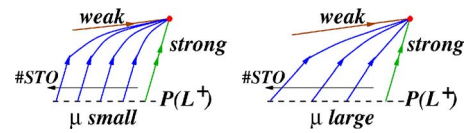

FIG. 6. (Color online) Within the singular funnel, secondary canards form the boundaries of subsectors traversed by submaximal MMO solutions. The number of subsectors and their sizes depend on μ. For fixed parameters, trajectories within sectors located farther from the strong eigendirection ("strong") approach the weak eigendirection ("weak") more directly and undergo more STOs per period than trajectories closer to the strong eigendirection.

Assumption 3: Let $p^{\pm}$ denote the points on Γ where $\Gamma_a^{\pm}$ intersect $L^{\pm}$. One of $p^{\pm}$ is a folded node, while the other is a jump point.

Assumptions 1–3 set up the (local) structure needed for MMOs to exist. Whether they actually exist or not depends on the global behavior of trajectories. Henceforth, we assume that $p^+ \in L^+$ is a jump point, since that is always the case for Eq. (4) (see Ref. 6). Suppose that $p^- \in L^-$ is a folded node. Within S_a^-, there exists a sector of solutions of Eq. (6), called the *singular funnel* of p^-, that are funneled through p^- to the repelling surface S_r of the critical manifold. This sector is bounded on one side by a branch of the strong stable manifold of p^-, which is called the *strong canard*, and on the other side by L^-. See Fig. 4 for an illustration of the singular funnel.

To check for MMOs, we define a global return map $\Pi : P(L^+) \mapsto P(L^+)$ by $\Pi = P \circ \Pi^+ \circ P \circ \Pi^-$ in the singular limit, where $\Pi^{\pm} : P(L^{\mp}) \mapsto L^{\pm}$ are defined from the flow of Eq. (6) and $P(L^{\mp})$ are the projections along the fast fibers, defined below Assumption 1. Fixed points of Π, when they exist, are singular periodic orbits, which may correspond to MMOs or to relaxation oscillations of system (4). The following theorem guarantees the existence of MMOs in system (4) for sufficiently small ε if any initial condition within the funnel of the folded node is mapped back into the funnel by the global return map Π (see Fig. 5). Note that the existence of a singular periodic orbit follows immediately when this condition is satisfied, since all trajectories within the singular funnel are contracted to the folded singularity by the flow of Eq. (6) on S_a^-.

Theorem 2.1 (see Ref. 8): *Suppose that system (4) satisfies Assumptions 1–3. If $p^- \in L^-$ is a folded node and the segment Γ_a^- of the singular periodic orbit Γ lies in the interior of the singular funnel of p^-, then for ϵ sufficiently small, there exists a stable periodic orbit of MMO type 1^{s^*} for some $s^* > 0$.*

Remark 2.1: *If system (4) satisfies Assumptions 1–3 and $p^- \in L^-$ is also a jump point, then the existence of a periodic relaxation oscillation orbit follows for sufficiently small ϵ.[9]*

In this paper, we study not just the existence but also the form of MMOs that arise in system (4). Let λ_1, λ_2 denote the eigenvalues of the linearization of Eq. (6) about the folded node p^-, with $|\lambda_1| \leq |\lambda_2|$. The numbers of large excursions L and small oscillations s in an L^s MMO are related to $\mu := \lambda_1 / \lambda_2 \leq 1$ and the global flow of trajectories from L^- to S_a^+ and back to S_a^-. More precisely, the maximal number of STOs is

$$s^* = s(\mu) = \left[\frac{1 + \mu}{2\mu} \right], \tag{7}$$

where the right-hand side of Eq. (7) denotes the greatest integer less than or equal to $(1 + \mu)/(2\mu)$.[10] Observe from Eq. (7) that $s^* = 1$ for $1/3 < \mu \leq 1$. If $\mu \leq 1/3$, then $s^* > 1$. In this case, there exist $[(1 - \mu)/2\mu]$ *secondary canards*[10] that divide the singular funnel into subsectors. Trajectories entering these subsectors correspond to submaximal 1^s MMO patterns with $s < s^*$ (see Fig. 6).

Note that μ measures the relative rates of attraction to the folded node along the two stable eigendirections, given by the flow of Eq. (6). Thus, changes in μ affect the path along which trajectories of Eq. (6) are contracted to the folded node, and formula (7) for $s(\mu)$ quantifies how this effect impacts the features of the corresponding MMOs.

The following theorem describes how variation of a parameter that modulates the global return map Π can select different 1^s MMO patterns, with $s < s^*$.

Theorem 2.2 (see Ref. 8): *Suppose that system (4) satisfies Assumptions 1–3. Assume that there exist a parameter β in system (4), independent of μ, and a value β_0 such that for $\beta = \beta_0$, the segment Γ_a^- of the singular periodic orbit Γ coincides with a segment of the strong stable manifold of p^-. The following then holds, provided ε is sufficiently small: For each $1 \leq s < s^*$, there exists an interval J_s with length of order $O(\varepsilon^{(1-\mu)/2})$ such that if $\beta \in J_s$, then a stable 1^s MMO pattern exists.*

While Theorem 2.1 simply gives the existence of MMOs for some $s > 0$, for ε sufficiently small, Theorem 2.2 implies that a variety of 1^s MMO patterns exist. The result in Theorem 2.2 can be considered in terms of a quantity δ that measures the distance of the singular orbit Γ from the strong canard (the border of the singular funnel). This distance is measured along $P(L^+)$, which both Γ and the strong canard intersect (see Fig. 7 for an example). We define δ such that positive values of δ result when the singular orbit is in the interior of the singular funnel, where $\delta = 0$ corresponds to $\beta = \beta_0$ in Theorem 2.2. Theorem 2.2 implies that for ε suffi-
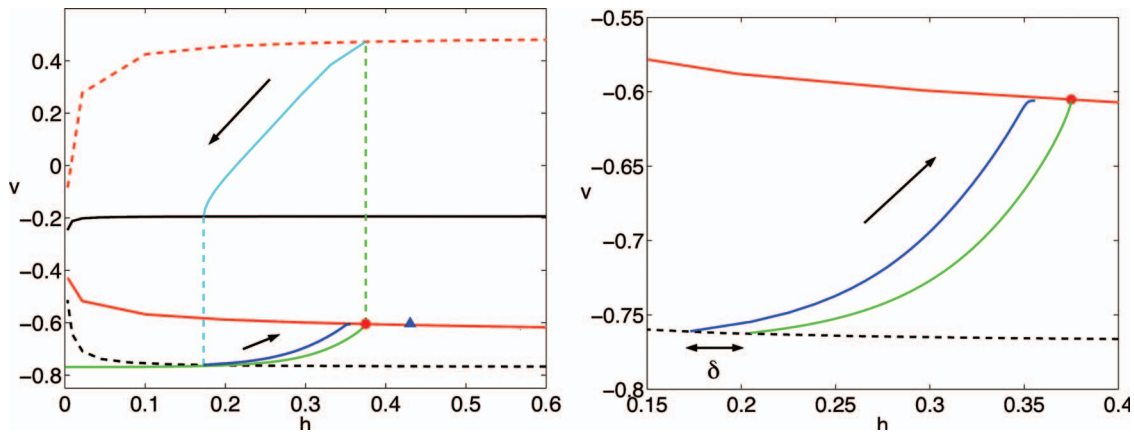
FIG. 7. (Color) Definition of δ using the global return map in the singular limit. Here, $\tau_h = 3$, $\tau_n = 1$, and $I = 8$, which gives MMOs. Left: Fold curves L^- (red solid), L^+ (black solid), $P(L^-)$ (red dashed), $P(L^+)$ (black dashed), strong canard (green solid), folded node of Eq. (6) (red circle), projection of the folded node to S_a^+ (green dashed), resulting flow in S_a^+ (cyan solid), projection of the trajectory from its intersection with L^+ to $P(L^+)$ (cyan dashed), and flow from that return back to a neighborhood of the folded node (blue solid), as defined from Eq. (6) and the projection P. The blue triangle is a saddle singularity of Eq. (6), and the arrows show the direction of flow. Since all points in the singular funnel are funneled through the folded node, the singular periodic orbit consists of the green dashed, cyan solid and dashed, and blue solid curves, along with the continuation of the latter up to the folded node. Right: A zoomed view illustrates the distance δ between the return point and the strong canard, in $P(L^+)$.

ciently small, different δ values give rise to different numbers $s < s^*$ of STOs, whereas $s = s^*$ is achieved for sufficiently large δ.

Remark 2.2: *We can achieve $\delta = 0$ in system (4) by varying I or τ_h. For I such that $\delta(I) = 0$, for example, the conditions of Theorem 2.2 are satisfied. However, we do not identify a specific parameter, such as I or τ_h, which plays the role of β in Eq. (4), because changes in each parameter lead to changes in μ as well as in δ, and therefore do not fulfill the condition that β is independent of μ. To vary δ without changing μ, we would have to define an auxiliary parameter depending on more than one of the parameters in Eq. (4).*

The selection of L^s patterns, with $L > 1$ and $s < s^*$, is less well understood. In the next sections, we will explore the impact of ϵ, I, and τ_h on the existence of MMOs as well as on $L \geq 1$ and s.

III. APPLICATION OF MMO THEORY TO EQ. (4)

In Ref. 6, we established that there exist $\tau_h^\ell > 1$ and $I_c > 0$ such that Eq. (4) satisfies Assumptions 1–3 whenever $\tau_h > \tau_h^\ell$, $\tau_n = 1$, and $I_c < I < I_r(\tau_h)$. The value $I_c \approx 4.8$ is determined as the bifurcation value above which Eq. (6) has a folded node. This value is independent of τ_h. The value $I_r(\tau_h)$ is the upper bound on the interval of I values within which the global flow maps points in the singular funnel back into the singular funnel. For $I = I_r(\tau_h)$, Γ_a^- coincides with a segment of the strong canard, with $\delta(I_r(\tau_h)) = 0$. The value $I_r(\tau_h)$ depends on τ_h, since the global flow itself does. For example, $I_r(\tau_h = 3) \approx 9.7$, while $I_r(\tau_h = 6) \approx 15.6$. The relation $I_c < I_r(\tau_h)$ holds precisely for $\tau_h > \tau_h^\ell \approx 1.3$. Qualitatively similar results are expected for other values of τ_n, but we fix $\tau_n = 1$ for concreteness.

Given that Assumptions 1–3 hold, MMOs exist for ϵ sufficiently small by either Theorem 2.1 or Theorem 2.2. However, once ϵ becomes positive, the values of I at which the onset and offset of MMOs occur may deviate from I_c and $I_r(\tau_h)$, respectively.

To explore more fully the dependence of onset and offset of MMOs on parameters, and to move beyond onset/offset to additional characteristics of the MMOs that exist, we systematically simulated system (4) over a range of (I, ϵ) values, for $\tau_h = 3$ and $\tau_h = 6$, using a fourth-order Runge-Kutta method implemented in XPPAUT[12] with a time step of ≤ 0.01 units. For a large number of particular parameter sets, we classified the resulting MMO solutions according to the numbers of subthreshold oscillations (s) and large excursions (L) present. We used these results to partition (I, ε) parameter space into regions in which different MMO patterns arise, using linear interpolation to generate solid boundary curves between regions based on a discrete set of data points. To avoid excessive partitioning of parameter space, it made sense to group $L = 3$ and $L = 4$ solutions together, so we let *few* denote 3 or 4. Given this, it is natural to let *more* denote 5 or more and to have a term meaning the complement of *more*, for which we selected *less*. The results of these simulations appear in Figs. 8 and 9.

To understand these and other $\epsilon > 0$ results, and to relate them to the singular $\epsilon = 0$ theory, we consider $\mu = \mu(I)$ and $\delta = \delta(I)$, as introduced in Sec. II. These quantities are defined in the singular limit; however, when we perturb away from the singular limit, corresponding quantities exist. In particular, there exists a near identity coordinate transformation that brings system (4) into the following normal form for a folded node, in which μ appears explicitly:[8]

$$\dot{x} = y - (\mu + 1)z + O(x, (y + z)^2, \varepsilon),$$

$$\dot{y} = \mu/2 + O(x, y, z, \varepsilon), \qquad (8)$$

$$\varepsilon \dot{z} = x + z^2 + O(xz^2, xyz, z^3) + \varepsilon O(x, y, z, \varepsilon).$$

Note that $\mu = \mu(I)$ in Eq. (8) is equivalent to $\mu = \lambda_1 / \lambda_2$ in Eq. (7), the quotient of the eigenvalues of the corresponding folded node, since eigenvalues are invariant under coordinate transformation. Therefore, we can define a perturbed param-
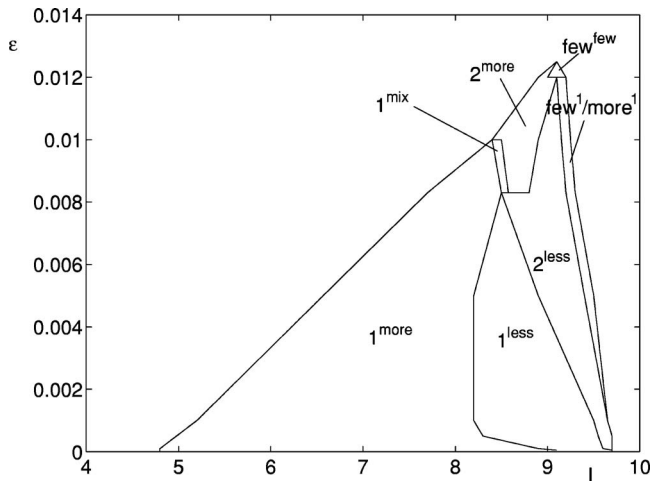
FIG. 8. Phase diagram for MMO solutions found numerically for Eq. (4), for $\tau_h=3$, $\tau_n=1$. Each label refers to the qualitative form of MMOs found in the corresponding region. We define *more* as any number greater than or equal to 5, *less* as any number less than 5, and *few* as 3 or 4. In the 1^{mix} region, we find that MMOs generally take the form $1^{s_1}11^{s_2}21^{s_1}1^{s_2}\ldots$, typically with $|s_1-s_2|>1$ in this particular region. Small pockets of such MMOs may also occur elsewhere in (I,ϵ) space, but we only find them over much smaller parameter ranges outside of the 1^{mix} region. Within the $\text{few}^1/\text{more}^1$ region, we find progressively more large excursions as I increases.

eter $\mu(I,\epsilon):=\mu(I)+O(\epsilon)$ in system (8), which characterizes the rotational behavior of the invariant manifolds in the same way that $\mu(I)$ does in the singular limit. Note that if $\mu(I)$ is large compared to the perturbation ϵ, then ϵ has only a weak influence on μ and hence on rotational properties. If μ is of the order of the perturbation ϵ, then the influence of ϵ becomes significant.

Similarly, we can define $\delta(I,\epsilon)$ by measuring the distance between a periodic solution and the strong canard solution, in a section in (v,h,n) space that is an appropriate perturbation of the curve $\{(v,h,n):(v,h)\in P(L^+),n$ satisfies Eq. (2) with $m=m_\infty(v)\}$.
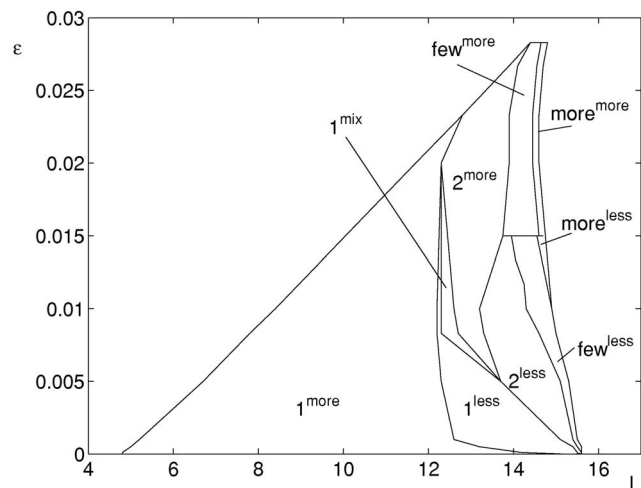

FIG. 9. Phase diagram for MMO solutions found numerically for Eq. (4), for $\tau_h=6$, $\tau_n=1$. The same terminology is used as in Fig. 8.

TABLE I. The onset of MMOs under variation of ε with $\tau_h=3$.

ε	$I_c(\varepsilon)$	$\mu(I_c(\varepsilon))$
0	4.9	0
0.001	5.2	0.0026
0.002	5.6	0.0057
0.004	6.3	0.011
0.006	7.0	0.015
0.0083	7.8	0.020
0.01	8.3	0.023

A. The influence of the perturbation ε on the onset of MMOs

In the singular limit $\varepsilon\to 0$, a folded singularity of Eq. (6) is classified as a folded node if $\mu>0$, and a folded saddle-node arises in the limiting case $\mu\to 0$. The folded saddle-node limit occurs at the onset of MMOs at $I=I_c$, and in this limit, the number s^* of maximal STOs tends to infinity ($\mu\to 0$) [see Eq. (7)]. The onset of MMOs is observed in Eq. (4) as a Hopf bifurcation, which can be located numerically, as I is increased in Eq. (4). However, the existence of a Hopf bifurcation in itself simply implies the existence of (small amplitude) oscillations, and the additional theory described in Sec. II must be invoked to account for MMOs.

Although the theory derived in the $\varepsilon\to 0$ singular limit predicts the onset of MMOs at $\mu=0$, Figs. 8 and 9 show that the I value at which the onset of MMOs occurs, call it $I_c(\varepsilon)$, is significantly increased under perturbations $\varepsilon>0$. Table I lists the values of ε and $I_c(\varepsilon)$, as well as $\mu(I_c(\varepsilon))$, for $\tau_h=3$, for a selection of ε values, including the value emerging from nondimensionalization of the original HH equations ($\varepsilon=0.0083$). Note that in Table I, the value $\mu(I_c(\varepsilon))$ is the value of μ, computed in the $\varepsilon=0$ limit, at the I value at which MMO onset is observed to occur for the values of ε shown.

To understand the mechanism for the ε dependence of I_c, recall that, as discussed above, the perturbation $\varepsilon>0$ can cause a shift in $\mu(I)$ values, from $\mu(I)$ to $\mu(I,\varepsilon)=\mu(I)+O(\varepsilon)$. Thus, for fixed $\varepsilon>0$, the onset condition $\mu(I,\varepsilon)=0$ could potentially occur at any I value such that $\mu(I)$, as computed in the singular limit, is an $O(\varepsilon)$ distance from 0.

Now, the onset of MMOs occurs as I increases in Eq. (4), which implies that $\mu(I,\varepsilon)$ is a monotonically increasing function of I near $I_c(\varepsilon)$, for each fixed ε. Numerically, we find that $\mu(I)$ is a monotonically increasing function on all of $(I_c,I_r(\tau_h))$. Furthermore, we find that $I_c(\varepsilon)$ is increasing monotonically. Hence, the onset of MMOs moves to values of I that had larger $\mu(I)$ values in the singular limit. This result implies that the perturbation to $\varepsilon>0$ causes negative shifts in μ; that is, $\mu(I,\varepsilon)<\mu(I)$ for fixed I. Therefore, for fixed ε, the excitable structure, for which Eq. (6) has a folded saddle [recall that a folded saddle is defined by $\mu(I)<0$] and a regular node, persists for $I_c<I<I_c(\varepsilon)$.

The sizes of the $\mu(I_c(\varepsilon))$ values in Table I are consistent with the claim that these are shifted to 0 by $O(\varepsilon)$ perturbations, yielding the shift of the onset of MMOs. The particularly strong shift shown in Figs. 8 and 9 is due to the fact that $\mu(I)$ is a very slowly increasing function, such that I has to

be increased significantly to cause an $O(\varepsilon)$ increase in μ. Within Figs. 8 and 9, the linearity of the dependence on ε of the $I_c(\varepsilon)$ value at which the onset of MMOs arises is clearly apparent. The mechanism responsible for this linearity remains to be explained precisely.

B. The influence of the perturbation ε on the offset of MMOs

As can be seen in Figs. 8 and 9, the value of I at which the offset of MMOs occurs, via a transition to regular relaxation oscillations, is much less strongly dependent on ϵ than is the onset value. When a folded node exists, either MMOs or relaxation oscillations may occur. The selection between MMOs and relaxation oscillations is determined by whether initial conditions within the singular funnel of the folded node return back to the singular funnel or not, under the global flow map Π. In the singular limit, this transition is defined by $\delta(I=I_r(\tau_h))=0$. We observe numerically that the global return mechanism here is relatively insensitive to ϵ, which gives rise to the weak effect of ϵ on $\delta(I,\varepsilon)=\delta(I)+O(\varepsilon)$.

C. The influence of the perturbation ε on the existence of maximal MMO patterns

Theorem 2.1 states that for sufficiently small ε and for $\mu>0$, 1^s MMO patterns with maximal STO number $s=s^*$ exist if the singular periodic orbit lies in the interior of the singular funnel of the folded node, away from the border of the singular funnel that is given by the strong canard of the folded node (i.e., if $\delta>0$ is not too small). In other words, if $\mu>0$ and $\delta>0$ are sufficiently bigger than the perturbation $\epsilon>0$, then the influence of the perturbation ε on the maximal MMO pattern obtained in the singular limit is negligible. Let us consider the relation between μ, δ, and ε under which Theorem 2.1 holds in more detail:

- $\mu=\mu(I)$ has to be bigger than $O(\sqrt{\varepsilon})$, i.e., $\mu(I)\gg\sqrt{\varepsilon}$ as $\varepsilon\rightarrow0$ is needed. This follows from the results on canards in $\mathbb{R}^3$ presented in Ref. 11. In a nutshell, the parameter μ scales with order $\sqrt{\varepsilon}$ in the geometric singular perturbation analysis of canards, rather than with order ε. If $\mu=O(\sqrt{\varepsilon})$, then the maximal number of STOs may be significantly perturbed away from s^*, and therefore Theorem 2.1 cannot hold. In the terminology of canards, a folded singularity that exists with $\mu=O(\sqrt{\varepsilon})$ corresponds to a folded saddle-node type singularity, as is defined by $\mu=0$ in the singular limit.
- $\delta=\delta(I)$ has to be bigger than $O(\varepsilon^{(1-\mu)/2})$, i.e., $\delta(I)\gg\varepsilon^{(1-\mu)/2}$ as $\varepsilon\rightarrow0$ is needed. This follows from the analysis on MMOs done in Ref. 8. In the singular limit, the entire singular funnel gives maximal STOs. That is, the border of the maximal subthreshold region is the strong canard itself, at $\delta=0$. Theorem 2.2 results because for ε sufficiently small but nonzero, the border becomes a sector of size $O(\varepsilon^{(1-\mu)/2})$, near the strong canard. This sector is divided into subsectors, bordered by secondary canards, that allow the possibility of various MMO patterns, other than 1^s (see Fig. 6). If $\delta(I)\gg\varepsilon^{(1-\mu)/2}$, for ε sufficiently small, then the corresponding periodic orbit is sufficiently

TABLE II. Key MMO parameters δ and μ under variation of the applied current I with $\tau_h=3$.

I		$\delta(I)$	$\mu(I)$
4.9	(I_c)	0.112	0
5.0		0.104	0.001
7.0		0.052	0.015
7.8		0.020	0.020
9.0		0.007	0.027
9.7	$(I_r(\tau_h))$	0	0.031

far away from these subsectors, and a maximal MMO pattern is expected by Theorem 2.1. On the other hand, Theorem 2.2 applies if $\delta=O(\varepsilon^{(1-\mu)/2})$, for ϵ sufficiently small, and it implies that submaximal 1^s patterns, i.e., $s<s^*$, will arise for such δ.

Remark 3.1: Note that the size of the sector of submaximal canards, namely, $O(\varepsilon^{(1-\mu)/2})$, varies between $O(\varepsilon^{1/2})$, for $\mu\rightarrow0$, and $O(\varepsilon^{1/3})$, for $\mu\rightarrow1/3$, depending on $0<\mu<1/3$. Recall that the interval $(0,1/3)$ is the relevant range of μ values here, since for $\mu>1/3$, Eq. (7) gives $s^*=1$, such that there are no secondary canards, and the only MMOs are 1^1.

The above discussion illustrates that for fixed τ_h, the parameters ε and I crucially shape the observed MMO patterns, where I determines the important quantities $\mu=\mu(I)$ and $\delta=\delta(I)$ in the singular limit.

Now, let us consider what we know about μ as well as δ for Eq. (4). Recall that if all parameters other than I are held fixed, the singular theory predicts the possibility of MMOs on $I_c<I<I_r(\tau_h)$, where the folded node comes into existence at $I=I_c$, with $\mu(I_c)=0$. In fact, the folded node exists for values $I>I_r(\tau_h)$ beyond the transition to relaxation oscillations; it is the global return mechanism that causes a switch from MMOs to relaxation oscillations at $I_r(\tau_h)$. The value $\mu(I)$ appears to be a monotonically increasing function of I, as noted above. Table II shows some of these values for $\tau_h=3$.

Next, consider the distance parameter $\delta=\delta(I)$ with $\delta(I)\geq0$ on the interval $(I_c,I_r(\tau_h))$. Numerical experimentation suggests that $\delta(I)$ is a monotonically decreasing function of I, although we have no rigorous proof of this observation. Obviously, $\delta(I)$ is a decreasing function close to $I=I_r(\tau_h)$, since this is the transition value to relaxation oscillations with $\delta(I_r(\tau_h))=0$, but monotonicity on the whole interval $(I_c,I_r(\tau_h))$ cannot be guaranteed in general. Table II is consistent with the claim that $\delta(I)$ is indeed a monotonically decreasing function for $\tau_h=3$.

A necessary requirement for Theorem 2.1 to hold is that both $\mu(I)\gg\sqrt{\varepsilon}$ and $\delta(I)\gg\sqrt{\varepsilon}$ for fixed I and ε (since $\varepsilon^{(1-\mu)/2}\geq\sqrt{\varepsilon}$, by Remark 3.1). Since $\mu(I)$ is an increasing function while $\delta(I)$ is a decreasing function of I, the size of the interval $I_{\max}(\varepsilon)$ values of I values in $(I_c,I_r(\tau_h))$, where both conditions are fulfilled is a decreasing function of ε. In particular, there is a maximal $\varepsilon=:\varepsilon_0$ value such that the size of $I_{\max}(\varepsilon)$ tends to zero for $\varepsilon\rightarrow\varepsilon_0$. In the case of $\tau_h=3$, we can estimate a bound on the maximal ε_0 value from Table II.

TABLE III. I values associated with some particular MMO patterns for $\tau_h = 3$.

MMO	$I_{\epsilon=0.0001}$	$I_{\epsilon=0.001}$	$I_{\epsilon=0.002}$
1^6	8.8	8.0	7.8
1^5	9.0	8.2	8.0
1^4	9.1	8.4	8.2
1^3	9.2	8.7	8.6
1^2	9.4	9.0	8.9
1^1	9.6	9.3	9.2
2^1	9.64	9.6	9.5
3^1	9.667	9.64	9.6
1^0	9.67	9.65	9.62

At approximately $I=7.8$, the curves $\mu(I)$, $\delta(I)$ intersect, with $\mu(I) = \delta(I) = 0.02$. It follows that $\varepsilon_0 \ll [\mu(7.8)]^2 = 4 \times 10^{-4}$. Thus, we estimate that $\varepsilon < 10^{-5}$ is required such that Theorem 2.1 can hold for some I value within $(I_c, I_r(\tau_h))$, whereas Theorem 2.1 cannot apply for any particular I value if $\varepsilon > 10^{-5}$. Therefore, essentially all of the MMO patterns indicated in Fig. 8 (more precisely, those above the line $\varepsilon = 10^{-5}$) are considered as submaximal MMO patterns. Almost all of the MMO patterns shown in Fig. 9 ($\tau_h=6$) are considered submaximal as well, by the same argument. As we have discussed, if ε is sufficiently small, then the selection of submaximal canards is described by Theorem 2.2. But just how small ε must be for this result to hold is not clear. In the next section, we consider to what extent the characteristics of the MMO patterns that we observe, for $\tau_h = 3$ and $\tau_h=6$, are consistent with the subsector structure underlying Theorem 2.2.

IV. THE SELECTION OF MMOs

Numerical studies of how MMO patterns change under variation of parameters, such as the results presented in Figs. 8 and 9, offer a description of MMO selection. We next address the mechanisms underlying the selection of particular submaximal MMOs, within the region of parameter space where MMOs exist.

A. ε fixed

For fixed ϵ (sufficiently small) and fixed τ_h, we can pick out a fixed progression of L^s MMO patterns. For example, for each of the three pairs $(\epsilon, \tau_h) = (0.0001, 3)$, $(0.001, 3)$, $(0.002, 3)$, we obtained the progression of MMOs given in Table III by simulation of Eq. (4), using a Runge-Kutta method in XPPAUT, for varying I. Note that in some cases we reduced the time step from $dt=0.01$ to $dt=0.005$, or $dt=0.001$ to ensure numerical accuracy.

Several features of the data in Table III merit attention. The observed progression of L^s MMO patterns forms a Farey-like sequence $1^6 \rightarrow 1^5 \rightarrow \cdots \rightarrow 1^1 \rightarrow 2^1 \rightarrow 3^1 \rightarrow 1^0$ (see, e.g., Ref. 13 for an introduction to Farey sequences). Such a sequence will arise for any fixed (sufficiently small) ε. If $\varepsilon > 0.0024$, then the Farey sequence that we obtain features L^s MMOs with $L>1$ more prominently. For example, for fixed $\varepsilon=0.0025$, we find a Farey-like sequence of the form 1^s

$\rightarrow \cdots \rightarrow 1^1 \rightarrow 2^2 \rightarrow 2^1 \rightarrow 3^1 \rightarrow \cdots \rightarrow 12^1 \rightarrow 1^0$. This switch-like behavior near $\varepsilon=0.0024$, from the situation where $L \leq 3$ to L^1 patterns with L large, is a special feature that we have observed numerically for this particular problem, with $\tau_h > 1$.

How can we explain the appearance of such a Farey-like sequence, consisting of submaximal 1^s MMO patterns and L^1 MMO patterns? Theorem 2.2 shows that for $\varepsilon > 0$ sufficiently small, 1^s MMO patterns with $s < s^*$ are a consequence of the existence of secondary canards that form subsectors, with one such subsector associated with each of the observed 1^s MMO patterns, $1 \leq s < s^*$ (see Fig. 6). Since $\delta(I)$ is a decreasing function of I, as long as the subsector structure persists for a given ϵ, the return mechanism will sweep through all possible subsectors as I is increased, explaining a $1^s \rightarrow \cdots \rightarrow 1^1$ sequence.

For $\epsilon > 0$ sufficiently small, L^1 patterns with $L>1$ are only possible if the global return mechanism projects the corresponding trajectory exponentially close to the strong canard (the border of the funnel); i.e., within an $O(e^{-(1/\varepsilon)})$ neighborhood of the strong canard.[8,14] Obviously, an increased ε will promote the possibility of being in such a neighborhood. This is consistent with the data in Table III, which suggest that L^1 patterns arise over larger intervals of I values for larger ε. In the case of a 2^1 pattern, for example, a trajectory, after creating a large oscillation, is projected back exponentially close to the strong canard and creates another large oscillation by following the strong canard. Subsequently, the return mechanism projects the trajectory back into the (first) subsector corresponding to the secondary canards, such that an STO results and a 2^1 pattern is created. On the other hand, if after two large oscillations the return mechanism again projects the trajectory close enough to the strong canard, then an additional large excursion is possible, leading to a 3^1 pattern. Hence, L^1 patterns for larger L require δ to be closer to zero; i.e., very close to the transition to 1^0 patterns (relaxation oscillations). Since $\delta(I)$ decreases with I, a sequence $1^1 \rightarrow 2^1 \rightarrow \cdots \rightarrow L^1 \rightarrow 1^0$ is expected for increasing I, for each fixed ε. Together, these observations give an explanation, which is consistent with the results in Theorem 2.2 proved rigorously for ε sufficiently small, of the dependence on ε and I of the Farey-like sequence described in Table III, and of similar sequences of MMO patterns that appear for each fixed ε (see Figs. 8 and 9).

We note that for each s, there also exist alternating MMO patterns, consisting of sequences of simple 1^s and 1^{s-1} patterns, in the transition from a 1^s MMO to a 1^{s-1} MMO that occurs under variation of the parameter I. For example, in the case $\varepsilon=0.001$ and $I=8.52$, we observe a (periodic) $1^3 1^4 1^4$ pattern. Similarly, we observe alternating MMO patterns, consisting of sequences of simple L^1 and $(L+1)^1$ patterns, in each transition from an L^1 pattern to an $(L+1)^1$ pattern under variation of I. For example, in the case $\varepsilon=0.001$ and $I=9.634$, we observe a (periodic) $2^1 3^1$ pattern.

In Figs. 8 and 9, it is also evident that more exotic MMOs are promoted by increases in τ_h, as well as by increases in ϵ. Such patterns include those featuring larger L values, those featuring both $L>1$ and $s>1$, or those featuring combinations of different patterns [i.e., switching be-
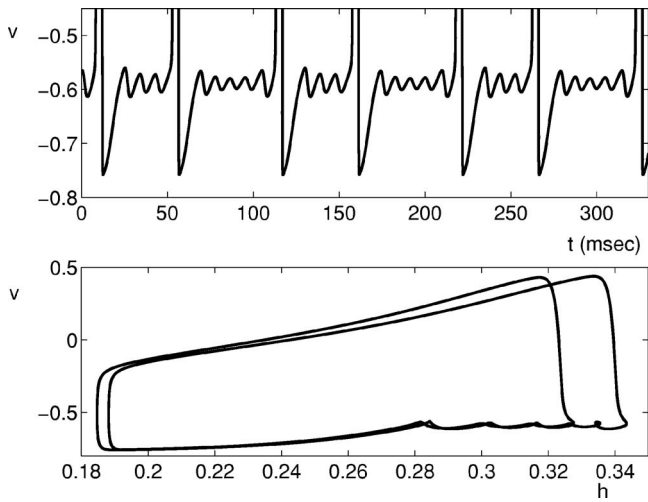
FIG. 10. An exotic MMO obtained from Eq. (4) with $\tau_h=6$, $\tau_n=1$, $I=12.6$, $\epsilon=0.0083$. This MMO features alternations of 1^3 and 1^5 patterns, as seen from the voltage trace in the top panel. The bottom panel shows the same solution projected to the (h,v) plane.

FIG. 11. MMO solutions of Eq. (4) for $\tau_h=3$ (top) and $\tau_h=6$ (bottom) for $\varepsilon=0.007$. From left to right: 1^9, 1^4, 2^3, and 3^1 MMOs.

tween L^s and $(L')^{s'}$ for either $|L-L'|>1, |s-s'|>1$, or both $|L-L'| \geq 1$ and $|s-s'| \geq 1$, as shown in Fig. 10, for example]. A theory to explain precisely the dynamical mechanisms responsible for all the observed exotic MMOs, such as the one shown in Fig. 10, has not yet been developed and is beyond the scope of this work. On the other hand, we can give an explanation of why increasing τ_h (for fixed ε) leads to more exotic MMOs.

Recall that a decreased μ value increases the number of subsectors associated with different numbers s of observed small oscillations in a L^s pattern, but the size of these subsectors decreases as μ decreases (see Remark 3.1 and Fig. 6). Since the size of the subsectors is decreased and the number increased, there will be more subsectors in a small (fixed size) neighborhood of the strong canard. This enhances the possibility that trajectories visit many of these different subsectors and more complicated MMOs occur. In particular, to observe periodic L^s patterns with both $L>1$ and $s>1$, the return mechanism has to bring trajectories very close to the strong canard at some time within each period; i.e., $\delta \approx 0$ is needed as well. The limiting values of $I_r(\tau_h)$ for the transition from MMOs to relaxation oscillations ($\delta=0$) are given, for example, by $I_r(\tau_h=3)=9.7$, $I_r(\tau_h=6)=15.6$, and $I_r(\tau_h=9)=18.9$. The corresponding μ values are given by $\mu(I_r(\tau_h=3))=0.031$, $\mu(I_r(\tau_h=6))=0.027$, and $\mu(I_r(\tau_h=9))=0.022$, which suggests that $\mu(I_r(\tau_h))$ is a decreasing function of τ_h. Therefore, we expect more exotic L^s patterns with both $L>1$ and $s>1$ for increased τ_h. If we increase τ_h from $\tau_h=3$ to $\tau_h=6$ for fixed $\varepsilon=0.002$, then we can find, for example, a $1^2 1^1 1^1 2^2$ MMO pattern for $I=14.5$, a 2^3 MMO pattern for $I=14.32$ (although this depends on initial conditions), and a $1^1 1^3$ MMO pattern for $I=14.0$. These patterns cannot be found for $\tau_h=3$ with $\varepsilon=0.002$. If we further increase to $\tau_h=9$ then we can also find, for example, a 4^1 MMO pattern for $I=18.7$, a 2^4 MMO pattern for $I=17.0$, and a $1^1 1^4$ MMO pattern for $I=16.6$ (again depending on initial conditions).

Figures 11 and 12 show examples of extremely similar MMO patterns, of matching types, produced with $\tau_h=3$ and
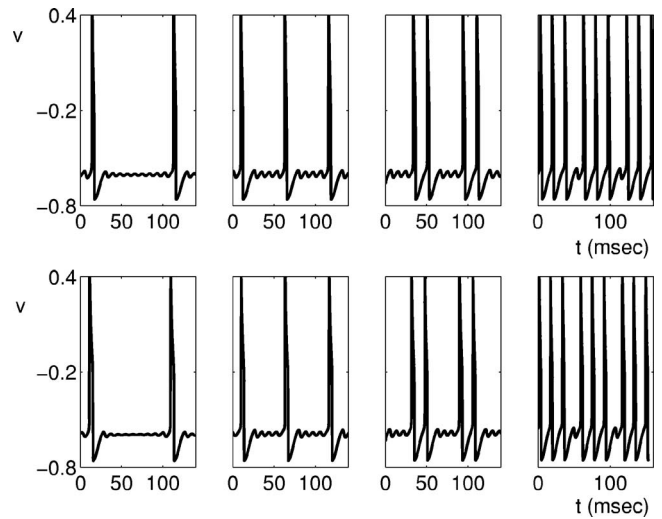
$\tau_h=6$, with $\varepsilon=0.007$, by selecting different values of I. In particular, for $\tau_h=3$, these patterns occur for $I=8$, 8.5, 9, 9.3, with $\mu(I)=0.021$, 0.024, 0.027, 0.029, respectively, while for $\tau_h=6$, the matching patterns occur for larger I values, namely, $I=11$, 12.5, 14, 14.8, with $\mu(I)=0.018$, 0.022, 0.025, 0.026. Figure 12 shows that for larger τ_h, there is a compression in the region of the phase space of Eq. (6) in which the subthreshold dynamics occurs for the same MMO type.

To understand the fact that larger I values are needed to produce a given MMO for larger τ_h, note that μ decreases as τ_h increases; e.g., $\mu(I,\tau_h=3) > \mu(I,\tau_h=6)$ for fixed I. Indeed, small μ reflects a large separation of timescales associated with the h and n dynamics, as can be induced by increasing
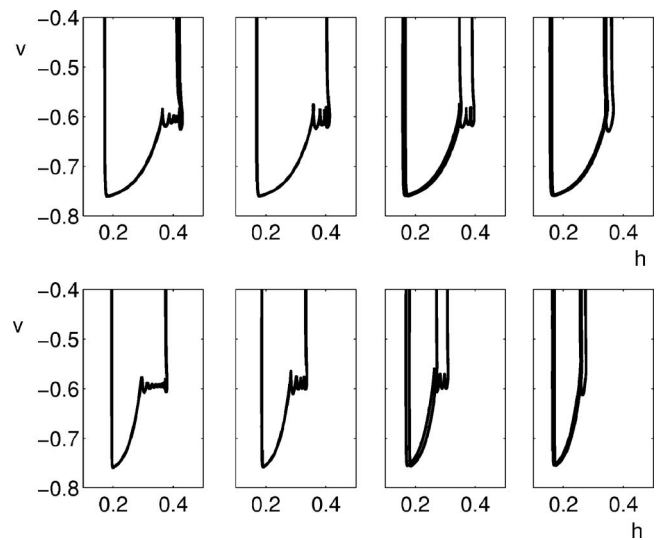

FIG. 12. Phase plane projections of MMO solutions of Eq. (4) shown in Fig. 11. These plots display, from left to right, 1^9, 1^4, 2^3, and 3^1 MMOs. They are zoomed in to show the return to the neighborhood of S_a^-, subthreshold oscillations that develop near L^-, and the jump away from S_a^-. In the top row, $\tau_h=3$, and in the bottom row, $\tau_h=6$. For each fixed MMO pattern shown, there is greater compression in the h (horizontal) direction for $\tau_h=6$, with smaller δ, than for $\tau_h=3$, as discussed in the text.
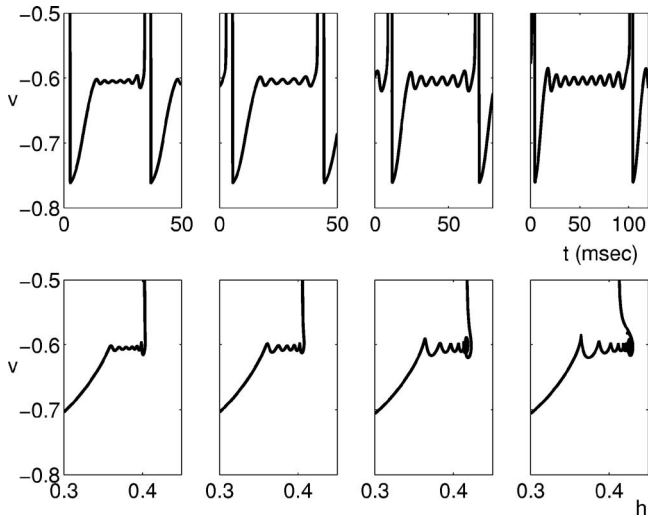
FIG. 13. MMOs for $\tau_h=3$, $\tau_n=1$, $I=8$, $\epsilon=0.001, 0.002, 0.0045, 0.007$, respectively. Note that the number of STOs per cycle decreases from 6 to 5 and then increases again as ϵ increases. Still larger numbers of STOs occur for $\epsilon<0.001$ as well; however, these are difficult to visualize due to their small amplitude. Indeed, the amplitude of STOs increases with ϵ.
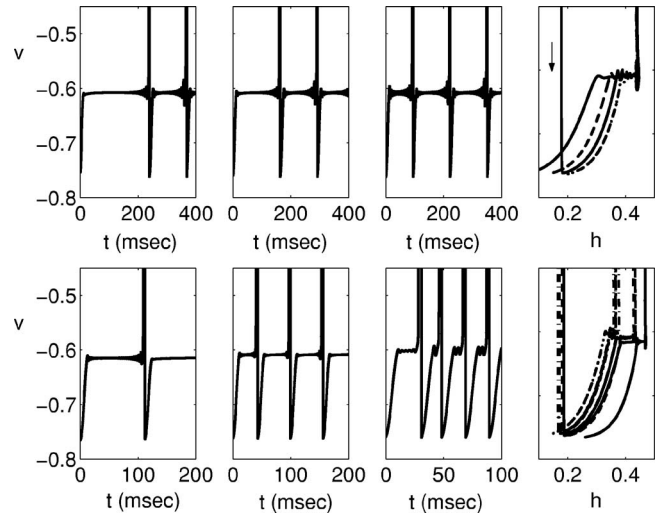

FIG. 14. MMOs selected by independent variation of δ and μ for $\tau_h=3$. Top: With $\varepsilon=0.004$ and $I=7$, initial conditions with different δ values lead to different numbers of STOs before the first large excursion. After this excursion, since all simulations share the same I and hence $\mu(I)$, identical MMOs result, with 13 STOs per cycle. From left to right: $\delta=0.2$ (solid in far right panel) gives approximately 20 STOs, $\delta=0.15$ (dashed in far right) gives approximately 17 STOs, $\delta=0.1$ (dash-dotted in far right) gives approximately eight STOs. The phase plane on the far right illustrates that different cases start with different h, yet all cases share the same global return (indicated by the arrow), leading to the same subsequent MMO pattern. Bottom: With $\varepsilon=0.001$, despite the fact that $\delta=0.025$ for all simulations shown, different initial numbers of STOs result for different I. Moreover, due to the different I and hence $\mu(I)$, different MMO patterns follow the initial large excursions in v. From left to right: $I=5.5$ (solid in far right panel) gives 26 STOs initially, $I=7$ (dashed in far right) gives eight STOs initially, $I=9$ (dash-dotted in far right) gives five STOs initially (although these are less tightly packed together in time than the $I=7$ STOs). The phase plane on the far right further illustrates the point that, due to the different I and hence $\mu(I)$, the different trajectories have different return positions.

τ_h from 1. Since $\mu=\lambda_1/\lambda_2$ for eigenvalues $\lambda_2<\lambda_1<0$ from linearization of Eq. (6) about the folded node, small μ is associated with an approach to the folded node closer to its weak eigendirection, which promotes more STOs. As a result, to obtain a fixed number of STOs for a larger τ_h, a smaller $\delta(I)$, and correspondingly, a larger value of I, is needed. These smaller $\delta(I)$ are evident in the compression seen in the phase planes for $\tau_h=6$, relative to those for $\tau_h=3$, in Fig. 12.

B. *I* fixed

Interestingly, for fixed I, a nonmonotonic change in the number of STOs within MMO patterns can be observed as ε is increased. For example, Fig. 13 displays the MMOs occurring for $I=8$ over a wide range of ϵ values, illustrating the decrease and subsequent increase in the number of STOs per cycle seen as ϵ increases. This nonmonotonicity appears to be fairly general, for fixed I in the 1^{more} region in Figs. 8 and 9. Furthermore, Figs. 8 and 9 show that as ε increases, the parameter set giving 1^{more} MMOs terminates at smaller I values, despite the fact that the onset of MMOs occurs for larger I values, such that the 1^{more} region shrinks from both sides. Similar trends occur for other regions. If we consider isoclines of particular 1^{more} patterns within the 1^{more} region in Figs. 8 and 9, we find curves that are qualitatively similar to the border between 1^{more} and 1^{less}, at least for ε not too large. The form of the isoclines reflects the two effects of increasing ε: (a) the shift of onset of 1^s patterns to larger I values and (b) the shift of transitions between patterns to smaller I values. Since there is a continuum of 1^s MMO patterns, the isoclines get squeezed for larger values of ε. Therefore, the isoclines vary nonmonotonically with ε, explaining the nonmonotonic behavior observed for fixed I.

C. Varying δ and μ independently

The above discussion explains how both the local characteristics of the flow of Eq. (6), such as μ, and the global return process, captured by δ, contribute to the selection of MMOs. Since this explanation, although it clarifies the relevant mechanisms, is not rigorous, we performed an additional set of simulations to examine further the roles of μ and δ. Specifically, we experimented with varying δ while holding μ, and all other parameters, fixed, and vice versa. Since $\mu=\mu(I)$ and $\delta=\delta(I)$ are *not* independent of each other (see Remark 2.2), we mimicked an independent variation of δ by choosing different initial conditions for system (4) on the projection curve $P(L^+)\subset S_a^-$ in (v,h,n) space, yielding different initial distances δ_0. When we varied δ_0, we counted the number of STOs before the first large voltage spike, since the trajectories that pass through the singular funnel end up contracted together, with details of initial conditions having little impact beyond the first passage. Our simulations showed that, consistent with the singular limit analysis behind Theorem 2.2 and the discussion in Sec. IV A, decreasing δ_0 decreases the number of STOs before the first excursion (and as expected has no impact on the number of STOs between subsequent excursions). Figure 14 shows voltage time courses for three sample simulations, illustrating this point.

From Remark 3.1 and Sec. IV A, however, we expect that the subsector sizes vary with μ. Thus, we cannot simply conclude that the distance δ, determined by the global return, selects the MMO pattern that will appear. To illustrate this further, we performed simulations using initial conditions that shared the same δ, for different I [and hence $\mu(I)$] values, with all other parameters fixed. We found that, despite the use of the same δ value, quite different numbers of STOs, before the first large excursion, resulted for different I values, as shown in Fig. 14. Indeed, smaller I values gave more STOs. This is consistent with the claim that smaller I values yield smaller μ, with smaller subsectors as well as stronger attraction to the weak eigendirection (Fig. 6), which pulls trajectories away from subsectors associated with submaximal, L^s, or exotic MMOs.

Remark 4.1: *Since the projection $P(L^+)$ lies at approximately constant v except when $h \ll 1$, we measured δ simply in terms of differences in h coordinates. We took care to ensure that all initial conditions really were on $P(L^+)$, so the error introduced by this approximation was quite small and did not account for the differences in STOs that occurred for fixed δ across different I values.*

From these simulations, we see that trajectories lying a fixed distance from the corresponding strong canards for different parameter sets may belong to different MMO sectors and yield different MMO patterns. Similarly, trajectories at different distances from their strong canards may yield similar MMO patterns, as in Figs. 11 and 12. In summary, $\delta(I)$, measured relative to the strong canard, does not determine MMO patterns on its own. Rather, the return position must be considered relative to a subsector structure, and both depend on I [via $\mu(I)$ for the subsectors in particular].

V. CONCLUSIONS

The variety of arguments in the previous sections may appear to paint a confusing picture about the existence and selection of MMO patterns for system (4) with $\tau_h > 1$. However, this picture can be summarized in terms of a few key results:

(1) In the singular limit $\varepsilon \to 0$, MMOs exist for $I_c < I < I_r(\tau_h)$ for $\tau_h > \tau_h^{e}$.[6] The folded node of Eq. (6) comes into existence as I increases through I_c, the value of which is independent of τ_h. The global return mechanism causes a switch from MMOs to relaxation oscillations at $I = I_r(\tau_h)$, which depends on τ_h.

(2) The existence of maximal 1^{s^*} MMOs for Eq. (4) predicted from the $\varepsilon \downarrow 0$ theory only extends to some interval of ε within $[0, 10^{-5})$. A wide variety of MMO patterns are expected for ε values above this interval.

(3) When all parameters are fixed, including $\varepsilon > 0$, MMOs exist on an interval $(I_c(\varepsilon), I_r(\tau_h; \varepsilon))$ of I values. The onset value $I_c(\varepsilon)$ and the offset value $I_r(\tau_h; \varepsilon)$ are $O(\varepsilon)$ perturbations of the values I_c, $I_r(\tau_h)$, respectively, defined in the singular limit. For fixed I in this interval, the MMO pattern that appears is strongly related to where trajectories from the singular funnel are mapped, under the global return to $P(L^+) \subset S_a^-$ induced by the flow of Eq. (4). This selection depends on more than the dis-

tance $\delta(I)$ between the return image and the strong canard, however. In analogy to the singular limit result in Theorem 2.2, it appears that the intervals in $P(L^+)$ that give rise to different numbers of STOs depend on a subsector structure that scales with $\mu(I)$ and ϵ (Fig. 6), as well as with τ_h. Thus, all of the control parameters that we have explored participate in MMO pattern selection, when MMOs exist.

(4) For fixed sufficiently small ε, we observe Farey-like sequences of MMOs, i.e., increases in I cause decreases in the number of STOs within 1^s MMO patterns, until a transition to L^1 patterns with increasing L occurs and finally the sequence terminates in a relaxation oscillation pattern. These trends can be understood through consideration of $\mu(I)$ and the distance $\delta(I)$ between initial conditions on $P(L^+)$ and the intersection of the strong canard with $P(L^+)$, as follows:

(a) As I, and hence $\mu(I)$, is increased, the rates of attraction to the folded node along the two stable eigendirections, given by the flow of Eq. (6), become more similar. Thus, when μ is larger, trajectories track the weak eigendirection less closely, yielding fewer STOs.

(b) It appears that $\delta(I)$ is a decreasing function of I. Thus, for larger I, the global return point is closer to the strong canard, which also leads to fewer STOs and promotes L^1 MMO patterns, with $L > 1$, if $\delta(I) \approx 0$.

Our work on MMOs in the Hodgkin-Huxley equations was motivated by the patterns observed numerically by Doi, Kumagai, and collaborators.[2–5] While these researchers tried to analyze these patterns using a fast-slow decomposition with one slow variable, the analysis in Eq. (6) shows that the HH system (1) fits within the framework of recently developed rigorous theory of MMO patterns in two-slow-variable singularly perturbed systems near folded nodes.[8,10] This theory can be used to approximate the regions in parameter space where MMOs will exist,[6] and it explains observed Farey-like sequences of MMO patters when the singular perturbation parameter ε is sufficiently small.

Since μ and δ tend to be small relative to ϵ for system (4), however, particularly as ε is made larger, L^s MMOs with both $L > 1$ and $s > 1$, and various exotic MMOs, can appear. For example, the case $\mu = O(\sqrt{\varepsilon})$ (or smaller) has to be considered as a folded saddle-node case (analogous to $\mu = 0$ in the singular limit). The general theory for MMO patterns in singularly perturbed systems near a folded saddle-node has yet to be developed and will be part of future work. In particular, we are interested in understanding how mixing of different 1^s MMOs (as shown in Fig. 10) as well as L^s MMOs, with both $L > 1$ and $s > 1$, may occur. A first approach to understanding the variety of (exotic) MMO patterns by a geometric singular perturbation analysis can be found in Ref. 14, where the authors study a prototypical example of a generalized canard mechanism for a system featuring three timescales. (Such a system has essentially a folded saddle-node structure.) For that prototypical example, the authors prove results on stable exotic MMO patterns con-

sisting of 1^s, 1^{s-1} and 1^{s-2} patterns as well as on stable 2^2 and L^1 patterns. Interestingly enough, we observe more exotic MMO patterns for system (4) than are seen in their prototypical three timescale example. Moreover, we find examples of abrupt, switch-like changes from L^s patterns with small L to those with large L as ε increases, as well as the appearance of multiple MMO patterns, selected by initial conditions, for certain fixed parameter sets. Complex MMO patterns have recently been identified and explained in systems with a weakly unstable saddle-focus, near a transition between sub- and supercriticality of an associated Hopf bifurcation.[15] Future studies will be needed to understand the exotic features that we have observed in the HH system (4) with $\tau_h > 1$.

The exotic MMOs observed in Figs. 8 and 9 for ε sufficiently far from 0 cannot be directly explained by the existing singular perturbation theory, simply because the perturbation is too strong. Nonetheless, the results that we observe are consistent with the trends given by the singular limit analysis, which suggests that at least at a qualitative level, the mechanisms that generate MMOs and contribute to MMO patterns for larger ε are closely related to those that are understood near the singular limit.

Another way to overcome the difficulty in the analysis related to large perturbation ε is to look at bifurcations of the full system (4) related to the onset of oscillations. For example, Guckenheimer et al.[16] have studied MMOs in the vicinity of codimension-2 subcritical Hopf-homoclinic bifurcations. In the singular limit, we obtain a homoclinic orbit in the case of a folded saddle-node, providing a theoretical opportunity for the existence of some form of Hopf-homoclinic bifurcation of the full system. The relationship of the phenomena we have analyzed in Eq. (4) to the work in Guckenheimer et al.[16] as well as to Shilnikov type homoclinic orbits requires further clarification, which remains for future work.

ACKNOWLEDGMENTS

APPENDIX: THE HODGKIN-HUXLEY MODEL

In the nondimensionalized HH system (1), the parameters are given by

$$\bar{I} = I/k, \quad \bar{g}_k = 0.3, \quad \bar{g}_l = 0.0025,$$

$$\bar{E}_{Na} = 0.5, \quad \bar{E}_K = -0.77, \quad \bar{E}_L = -0.544,$$

$$\epsilon = 0.0083,$$

where I is the applied current in the original HH model (in $\mu A/cm^2$), $k = (120 \text{ mS}/cm^2)k_v$, and $k_v = (100 \text{ mV})$. These values are obtained from those in Ref. 1 by a nondimensionalization process described fully in Ref. 6. Define

$$\alpha_m(v) = \frac{(k_v v + 40)/10}{1 - \exp(-(k_v v + 40)/10)},$$

$$\beta_m(v) = 4 \exp(-(k_v v + 65)/18),$$

$$\alpha_h(v) = 0.07 \exp(-(k_v v + 65)/20),$$

$$\beta_h(v) = 1/(1 + \exp(-(k_v v + 35)/10)),$$

$$\alpha_n(v) = \frac{(k_v v + 55)/100}{1 - \exp(-(k_v v + 55)/10)},$$

$$\beta_n(v) = 0.125 \exp(-(V + 65)/80),$$

each with units of $(ms)^{-1}$. Additional functions in the model are

$$x_\infty(v) = \frac{\alpha_x(v)}{\alpha_x(v) + \beta_x(v)}$$

for $x \in m, h, n$ and

$$t_x(v) = \frac{k_t}{\alpha_x(v) + \beta_x(v)},$$

with $k_t = 1$ ms, such that each t_x is dimensionless. Finally, $\tau = t/k_t$, where t is the original time variable, in milliseconds, in Ref. 1.

[1] A. L. Hodgkin and A. F. Huxley, "A quantitative description of membrane current and its application to conduction and excitation in nerve," J. Physiol. (London) **117**, 500 (1952).

[2] S. Doi and S. Kumagai, "Nonlinear dynamics of small-scale biophysical neural networks," in *Biophysical Neural Networks: Foundations of Integrative Neuroscience*, edited by R. Poznanski (Mary Ann Liebert, New Rochelle, NY, 2001).

[3] S. Doi, S. Nabetani, and S. Kumagai, "Complex nonlinear dynamics of the Hodgkin-Huxley equations," Biol. Cybern. **85**, 51 (2001).

[4] S. Doi, J. Inoue, and S. Kumagai, "Chaotic spiking in the Hodgkin Huxley nerve model with slow inactivation of the sodium current," J Integr Neurosci **3**, 207 (2004).

[5] S. Doi and S. Kumagai, "Generation of very slow rhythms and chaos near the Hopf bifurcation in single neuron models," J. Comput. Neurosci. **19**, 325 (2005).

[6] J. Rubin and M. Wechselberger, "Giant squid—hidden canard: the 3D geometry of the Hodgkin-Huxley model," Biol. Cybern. **97**, 5 (2007).

[7] N. Fenichel, "Geometric singular perturbation theory," J. Differ. Equations **31**, 53 (1979).

[8] M. Brøns, M. Krupa, and M. Wechselberger, "Mixed mode oscillations due to the generalized canard phenomenon," Fields Inst. Commun. **49**, 39 (2006).

[9] P. Szmolyan and M. Wechselberger, "Relaxation oscillations in $\mathbb{R}^3$," J. Differ. Equations **200**, 69 (2004)

[10] M. Wechselberger, "Existence and bifurcation of canards in $\mathbb{R}^3$ in the case of a folded node," SIAM J. Appl. Dyn. Syst. **4**, 101 (2005).

[11] P. Szmolyan and M. Wechselberger, "Canards in $\mathbb{R}^3$," J. Differ. Equations **177**, 419 (2001).

[12] B. Ermentrout, *Simulating, Analyzing, and Animating Dynamical Systems* (SIAM, Philadelphia, PA, 2002).

[13] G. H. Hardy and E. M. Wright, *An Introduction to the Theory of Numbers*, 5th ed. (Oxford University Press, New York, 1979).

[14] M. Krupa, N. Popovic, and N. Kopell, "Mixed-mode oscillations in three time-scale systems: a prototypical example," preprint (2007).

[15] G. Medvedev and Y. Yoo, "Multimodal oscillations in systems with strong contraction," Physica D **228**, 87 (2007).

[16] J. Guckenheimer, R. Harris-Warrick, J. Peck, and A. Willms, "Bifurcation, bursting, and spike frequency adaptation," J. Comput. Neurosci. **4**, 257 (1997).